

Orogenic-wedge deformation and potential for great earthquakes in the central Andean backarc

Benjamin A. Brooks^{1*}, Michael Bevis², Kelin Whipple³, J Ramon Arrowsmith³, James Foster¹, Tomas Zapata⁴, Eric Kendrick², Estella Minaya⁵, Arturo Echalar⁶, Mauro Blanco⁷, Pablo Euillades⁷, Mario Sandoval⁶ and Robert J. Smalley Jr⁸

Subduction of the Nazca plate beneath South America has driven the growth of the Andes Mountains. Subduction has routinely generated earthquakes larger than magnitude 8.0 along the western margin of the mountain belt¹, but the potential size of less frequent earthquakes in the eastern, backarc margin is unknown. Continued support of the high Andean Plateau at the centre of the Andes can be explained only if deformation of the backarc margin is ongoing^{2–4}. Here we present GPS data that record surface motions in the Subandean ranges that are part of the backarc margin. We find that the velocity of surface movement decreases sharply from west to east across the Subandean ranges. We suggest that a subhorizontal fault underlying the ranges slips freely at depth in the west, but is locked for up to 100 km in shallower sections further east. Analysis of fault scarps formed where the subhorizontal fault intersects the surface indicates that the fault has generated repeated large earthquakes. We suggest that rupture of the entire locked section of the fault could generate an earthquake of magnitude 8.7–8.9. We attribute the large seismic potential to the unusual width of the Subandean ranges, and suggest that deformation of the Subandean ranges, at a rate unmatched by erosion, causes the mountain range to widen.

The central Andean Plateau (AP) is a bilaterally symmetric plateau of ~4,000 m average elevation (Fig. 1). Although AP uplift scenarios are currently debated^{5,6} it is generally accepted that the backarc orogenic wedge on the AP's east flank, comprising the Eastern Cordillera (EC), Inter-Andean zone (IAZ), and Subandes (SA), has contracted by more than ~250 km since ~45 Myr ago (refs 7–9). Wedge deformation has been facilitated by the presence of weak, subhorizontal decollement horizons in a 6–12 km thick pile of Palaeozoic marine sediments⁷, the along-strike continuity of which gives the southern SA (SSA) its long, narrow anticline-cored ridges (Fig. 1b). Across-strike, the SSA is more than 100 km wide and workers have appealed to coupled tectonics and erosion models to suggest that a dry climate over millions of years promoted the relatively large width¹⁰.

Modern geodetic studies document ~63 mm yr⁻¹ of Nazca–South America convergence at the latitude of the AP, a rate that has decelerated over the past 10–20 Myr (ref. 11). Near the Chile trench, ephemeral locking and release of the main plate

interface as part of the subduction earthquake cycle dominates the surface displacement field^{12,13}. In the backarc, plate boundary locking also significantly contaminates the velocity field along much of the Andes¹⁴. The AP's east flank in Bolivia, however, is located ~500 km inland, far enough that plate boundary locking contributes less than 10% to the measured velocity (<~1 mm yr⁻¹), allowing the orogenic wedge's velocity field to be isolated¹³. Because the early GPS measurements in the backarc were spatially sparse, interpretation with respect to wedge-specific processes has been limited¹⁵.

In a South America fixed reference frame, we present a new GPS velocity field for the backarc derived from reoccupations of the network that we augmented in 2000 and 2003 (Fig. 1, Supplementary Information S1). Although the velocity magnitude decreases away from the trench and vectors are subparallel to Nazca–South America convergence, as expected, the new results demonstrate a sharp backarc velocity decrease from ~10 to ~2 mm yr⁻¹ over ~25–100 km (Fig. 2). The velocity gradient is offset by ~100 km to the west from the topographic front of the SSA and we model it as a single dislocation in an elastic half-space that approximates a frictional stability transition on the basal decollement from freely slipping (towards the mountain interior) to fully locked (towards the craton). We compare model and data using Monte-Carlo based methods and do not model fault geometry variations in the trench parallel direction, allowing reduction of the number of free parameters to six: width of the locked zone (W_L , equivalent to distance from the deformation front), depth to the lower boundary of the locked zone (Z), dip (*dip*), strike (*strike*), strike-slip (U_1), and dip-slip (U_2) (Supplementary Information S2). Because we use only horizontal velocities in our inversion, Z is more poorly constrained than if vertical velocities were used¹⁶. We mitigate this by using balanced cross-sections from the region^{7–9} to assign an a priori constraint on Z of 10 ± 5 km.

The well-constrained parameter distributions (Fig. 2a–f) demonstrate that, at better than 95% confidence, the decollement is gently west-dipping (<5°), slipping at rates of 9–13 mm yr⁻¹ (U_2) and 1–3 mm yr⁻¹ (U_1 dextral), and that its locked width, W_L , is ~85–100 km. The estimated dip-slip range agrees with Quaternary geologic shortening rate estimates of 7–10 mm yr⁻¹ (refs 17,18; because the geologic estimates assume plane-strain it

¹School of Ocean and Earth Science and Technology, University of Hawaii, 1680 East-West Rd., Honolulu, Hawaii 96822, USA, ²School of Earth Sciences, The Ohio State University, 125 S. Oval Mall, Columbus, Ohio 43210, USA, ³School of Earth and Space Exploration, Arizona State University, PO Box 871404, Tempe, Arizona 85287, USA, ⁴YPF Services USA, 1330 Lake Robbins Drive, Box 10, The Woodlands, Texas 77380, USA, ⁵Observatorio San Calixto, Calle Indaburo 944, Casilla 12656, La Paz, Bolivia, ⁶Instituto Geografico Militar, Av Saavedra 2303, La Paz, Bolivia, ⁷Instituto CEDIAC, Universidad Nacional de Cuyo, Centro Universitario, Parque General San Martín. CC 405–(5500) Mendoza, Argentina, ⁸Center for Earthquake Research and Information, The University of Memphis, 3876 Central Ave., Suite 1, Memphis, Tennessee 38152-3050, USA. *e-mail: bbrooks@hawaii.edu.

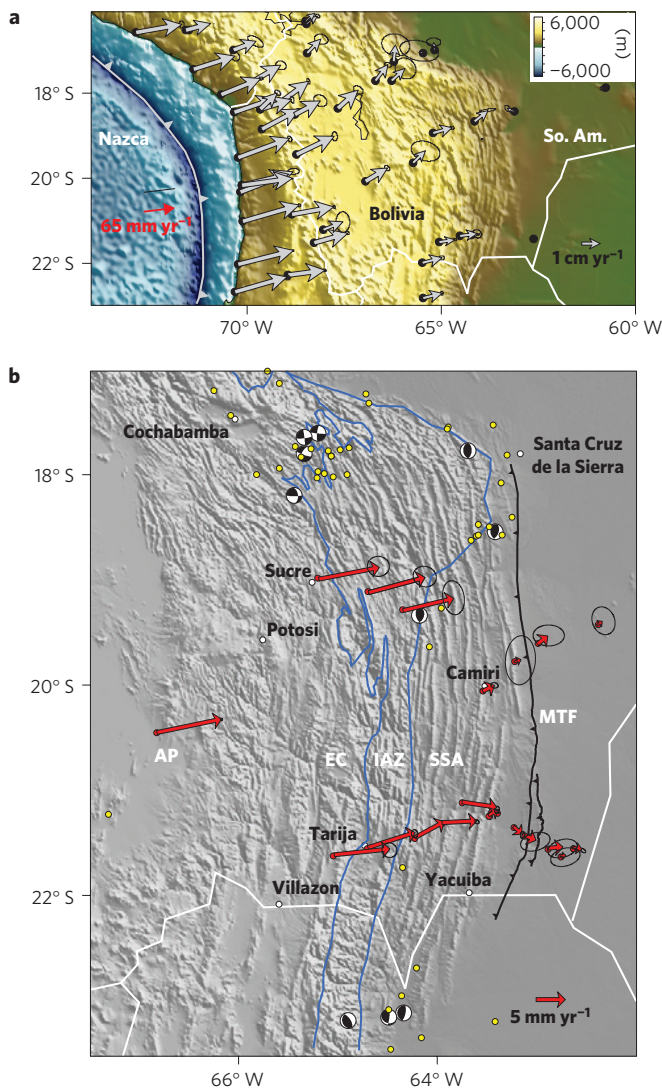


Figure 1 | GPS velocity fields in a South America-fixed reference frame.

a, Topography of the central Andes and regional velocity field (grey vectors) from ref. 13. Black arrow, Nazca–South America plate convergence vector. Grey triangles, trace of Nazca–South America subduction boundary, pointing in the down-dip direction. **b**, Shuttle Radar Topographic Mission (SRTM) topography and new velocity field from the SSA (red vectors). All error ellipses are 2σ . Focal mechanisms are for crustal events (<33 km) in the Global Centroid Moment Tensor (CMT) database with magnitudes that range from 4.9 to 6.6. Yellow circles, National Earthquake Information Center (NEIC) epicentres for crustal events. Blue lines, limits of physiographic provinces. AP, Andean Plateau; EC, Eastern Cordillera; IAZ, Inter-Andean zone; SSA, southern Subandes. Black triangles, trace of Mandeyapeca thrust fault (MTF), pointing in the down-dip direction.

is appropriate to compare only with U_2 estimates). In comparison to other active wedges, estimated W_L for the SSA is ~ 1.5 times as large as Taiwan, where there is a history of $\sim M_w$ 7 decollement earthquakes¹⁹, and it is equivalent to estimates from the Himalayan wedge, where earthquakes up to M_w 8.4 have been inferred^{16,20}. Furthermore, for quartzo-feldspathic rocks, the slipping-to-locked transition where frictional behaviour changes from velocity-strengthening (promoting continuous creep) to velocity-weakening (promoting stick-slip) is typically close to ~ 300 °C (ref. 21), and our analysis agrees well with this relation: the 300 °C contour from a recent comprehensive determination of the SSA geothermal gradient²² intersects the decollement

within the 95% confidence region of the estimated slipping-locked transition (Fig. 2g).

How continuously accumulating slip is released along the locked portion of the decollement is critical in determining the wedge's seismic potential. Owing to their velocity weakening properties, fully locked fault patches typically exhibit stick-slip behaviour²¹, leading us to expect that, as in other seismically active wedges, earthquakes in the SSA could episodically relieve the accumulated slip^{16,19}. Along the Himalayan front, for instance, where the geodetically estimated accumulation rate is equivalent to the Holocene slip rate in the frontal Siwalik hills²³, the total amount of accumulated slip is apparently transferred to the wedge front in earthquakes that rupture the entire locked width and cause shallow fault-related folding and/or surface ruptures²⁰. Along the SSA front, because there is no suitable Holocene chronostratigraphy with resolving power at the 100–1,000 yr repeat times of typical seismic cycles, we cannot quantify the relative probability of accumulated slip propagating to the thrust front versus activation of any other structure in the locked zone. Identification of multiple $\sim N-S$ trending fault scarps associated with the mapped trace of the ~ 500 km long Mandeyapeca thrust fault (MTF; ref. 24; Figs 1, 3), however, combined with the lack of surficial neotectonic evidence associated with any of the other SSA structures, strongly suggests that the most recent events have seismically ruptured the wedge front.

Closer examination reveals that the MTF surface expression is divided into five topographic segments (Fig. 3a), exhibiting relief profiles characterized by central maxima tapering towards \sim zero-valued inflection points that may indicate persistent rupture segmentation (Fig. 3b, Supplementary Information S4). For each segment we consider a range of rupture aspect ratios and use standard scaling relations²⁵ to estimate that potential earthquake magnitudes range from M_w 7.2–8.3 (Fig. 3b, Supplementary Information S5). Given the small spatial scale of the segment boundaries, it is likely that they are not substantial enough to act as barriers for all dynamic ruptures²⁶ and it is reasonable to consider that a single earthquake could rupture the entire MTF. In this endmember scenario, if the entire locked width, W_L , of the decollement were to rupture, we estimate a maximum slip of ~ 10 m (Fig. 3c) and M_w values as high as 8.7–8.9 (Fig. 3d). These are probably conservative estimates: 10 m may be a low value for coseismic slip given the recent interpretation of much larger single-event slip magnitudes from palaeoseismic investigations of the Himalayan thrust front²⁰. Furthermore, it is possible that coseismic rupture could extend below the lower boundary of the locked zone²¹. For both segmented and non-segmented rupture scenarios, the amount of time needed to accumulate the necessary amount of fault slip ranges between ~ 150 and 1,000 years (Fig. 3b,e), although if as-yet-undetected slow slip events occur on the decollement then recharge estimates could be longer. Considering the complicated way in which stress from accumulating slip and before-slip events is distributed on the decollement, we cannot determine how close to failure the MTF system is, although we can make valuable estimates. The earthquake catalogue is expected to be complete for M_w 7–8 since 1886 and 1700, respectively²⁷, and no events this size have been reported. Thus, it is likely that enough slip has accumulated since 1886 for a $\sim M_w$ 7 rupture.

The potential for great backarc earthquakes in the SSA stems from the large fault area available for seismic rupture. Along strike, fault rupture dimension is controlled primarily by the stratigraphic continuity of the Palaeozoic decollement horizons⁷. To better understand the physical controls on across-strike rupture dimension (measured by W_L) we appeal to critical taper theory²⁸, which states that to attain a steady-state width, a deforming

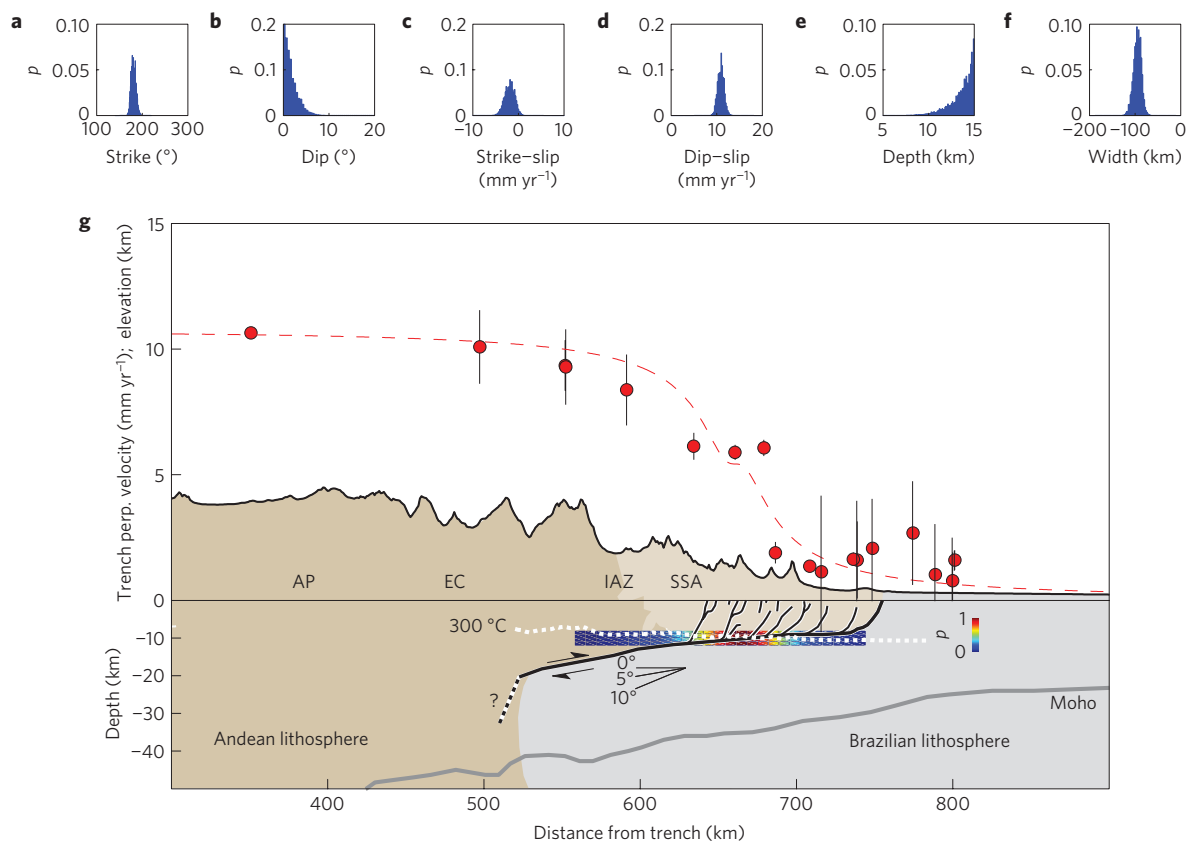


Figure 2 | Marginal posterior probability distributions (PPDs) for estimated dislocation parameters and a cross-section at 20° S. a, strike, (b), dip, (c), strike-slip (dextral, negative), (d), dip-slip, (e), depth, (f), locking width, W_L . g, Red circles, trench-perpendicular component of all new GPS velocities from Fig. 1b with 2σ error bars. Red dashed line, best model from inversion (strike, 181°; dip, 0.1°; strike-slip, -1.5 mm yr^{-1} ; dip-slip, 11.1 mm yr^{-1} ; depth, 14.9 km; W_L , 94 km). Black lines, topographic profile. Rainbow shading, PPD for W_L at 10 km depth. Black lines in subsurface, faults from regional cross-section¹⁸. White dashed line, 300 °C isotherm calculated from the geothermal gradient²².

orogenic wedge must reach a mass balance between accretionary flux, F_A , into, and erosional flux, F_E , out of, the wedge. Non-steady wedges that have greater F_A , lesser F_E , or are underlain by lower friction decollements, will strive towards larger widths by means of cratonward propagation of the wedge tip, which will also lead to an increase in W_L . We can evaluate the mass balance in the SSA. From our geodetically estimated slip rate ($\sim 9\text{--}13 \text{ mm yr}^{-1}$) and published Quaternary shortening rates ($7\text{--}10 \text{ mm yr}^{-1}$; refs 17, 18), and assuming an accretionary thickness of $\sim 10 \text{ km}$ from the balanced cross-sections, we estimate F_A ($\sim 70\text{--}130 \text{ m}^2 \text{ yr}^{-1}$) to be significantly larger than F_E estimates ($\sim 50 \text{ m}^2 \text{ yr}^{-1}$) determined from SSA-wide denudation rates over similar time periods²⁹ ($10^2\text{--}10^6$ years, Supplementary Information S3). Thus, unless the excess mass is accommodated by active, as yet undetected Quaternary shortening in the IAZ or EC to the west, the SSA has been in a transient state that favours widening. The non-steady conditions have probably persisted since at least $\sim 6 \text{ Myr}$ ago, when the wedge front began propagating rapidly towards the craton, in concert with an increase in SSA shortening rate from ~ 1.5 to $\sim 11 \text{ mm yr}^{-1}$ (ref. 18). During that same time, there is no evidence to suggest that F_E would have decreased: on the contrary, SSA precipitation rates (and, presumably erosion rates) seem to have steadily increased despite the generally dry climate^{6,30}. We infer, therefore, that the great seismogenic potential in the SSA is attributable to some combination of an increase in accretionary flux and material properties (stratigraphic architecture and thermal gradient) that have governed the growth of the contractional wedge and the depth of the transition to velocity-strengthening behaviour.

This paper has focused on the physical processes governing orogenic wedge deformation and seismicity that are elucidated by the new geodetically defined surface velocity field and existing SSA topography. Of more pressing import, however, is that the SSA is host to a population of more than two million people and associated infrastructure that, our analysis shows, are exposed to significantly underestimated seismic hazard. Owing to its relative quiescence, the most recently published seismic hazard assessment for the SSA considers the maximum expected earthquake size to be M_w 7.5 (ref. 27), in comparison to our estimates of M_w 8.7–8.9 (Fig. 3d).

Received 8 October 2010; accepted 30 March 2011;
published online 8 May 2011

References

1. Kanamori, H. The energy release of great earthquakes. *J. Geophys. Res.* **82**, 2981–2987 (1977).
2. Isacks, B. L. Uplift of the central Andean plateau and bending of the Bolivian orocline. *J. Geophys. Res.* **93**, 3211–3231 (1988).
3. Lamb, S. & Davis, P. Cenozoic climate change as a possible cause for the rise of the Andes. *Nature* **425**, 792–797 (2003).
4. Oncken, O. *et al.* in *The Andes Frontiers in Earth Sciences* (eds Oncken, O. *et al.*) Ch. 1, 3–27 (Springer, 2007).
5. Garzione, C. N. *et al.* Rise of the Andes. *Science* **320**, 1304–1307 (2008).
6. Ehlers, T. A. & Poulsen, C. J. Influence of Andean uplift on climate and paleoaltimetry estimates. *Earth Planet. Sci. Lett.* **281**, 238–248 (2009).
7. Dunn, J. F., Hartshorn, K. G. & Hartshorn, P. W. in *Petroleum Basins of South America AAPG Memoir Vol. 62* (eds Tankard, A. J., Suarez Soruco, R. & Welsink, H. J.) 523–543 (1995).
8. Baby, P., Rochat, P., Mascle, G. & Herail, G. Neogene shortening contribution to crustal thickening in the back arc of the Central Andes. *Geology* **25**, 883–886 (1997).

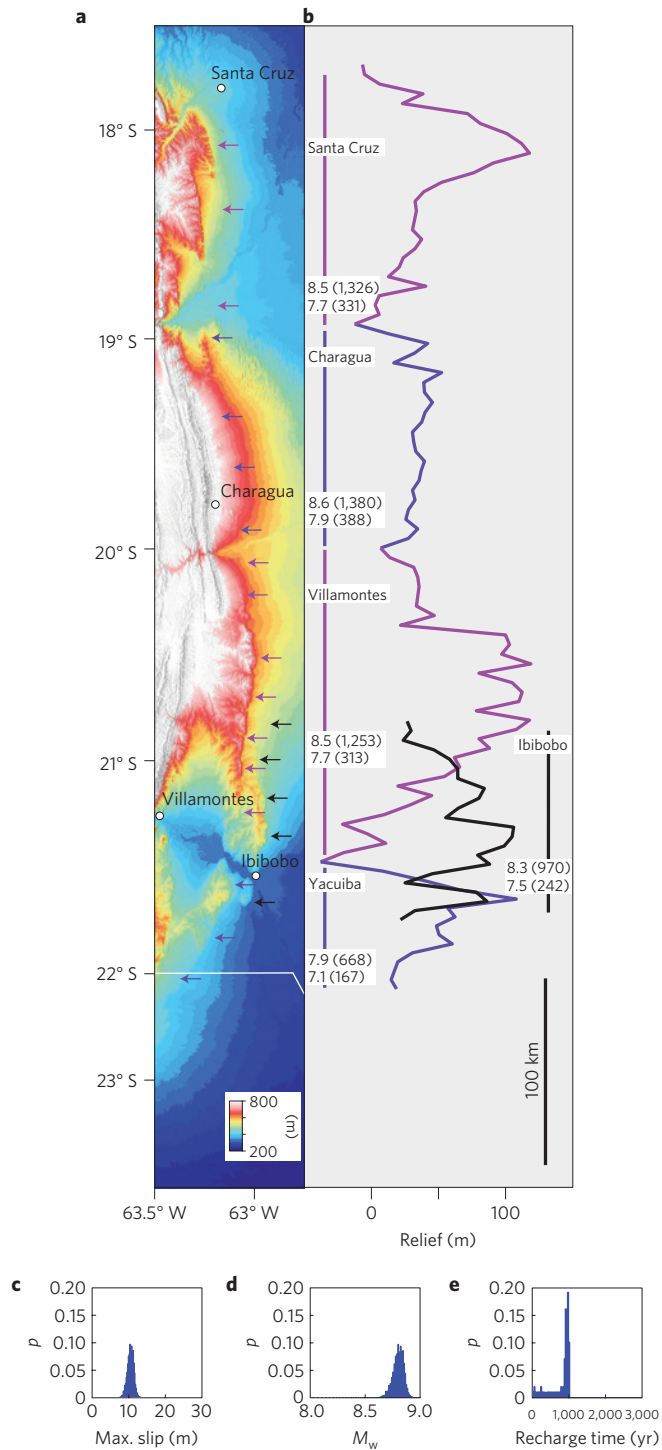


Figure 3 | Topographic analysis of the Mandeyapecua Thrust Front and estimated maximum earthquake parameters. a, SRTM Topography. Coloured arrows, segment fault traces; colours correspond to **b**. See also Supplementary Figures S13–8. **b**, MTF relief (median hanging wall minus median footwall elevation). Vertical coloured bar indicates estimated range of M_w and recharge time, in parentheses, for each segment. **c–e**, derived parameters: maximum slip (**c**), moment magnitude, M_w (**d**), and recharge time (**e**, slip rates taken from Fig. 2d) for the case where rupture is of the entire locked width (taken from Fig. 2f) and entire length of the MTF.

- McQuarrie, N. The kinematic history of the Central Andean fold-thrust belt, Bolivia; implications for building a high plateau. *Geol. Soc. Am. Bull.* **114**, 950–963 (2002).
- Masek, J. G., Isacks, B. L., Gubbels, T. L. & Fielding, E. J. Erosion and tectonics at the margins of continental plateaus. *J. Geophys. Res.* **99**, 13941–13956 (1994).
- Kendrick, E. *et al.* The Nazca–South America Euler Vector and its rate of change. *J. S. Am. Earth. Sci.* **16**, 125–131 (2003).
- Norabuena, E. *et al.* Space geodetic observations of Nazca–South America convergence across the Central Andes. *Science* **279**, 358–362 (1998).
- Bevis, M. *et al.* On the strength of interplate coupling and the rate of back arc convergence in the central Andes: An analysis of the interseismic velocity field. *Geochem. Geophys. Geosyst.* **2**, 1067 (2001).
- Brooks, B. *et al.* Crustal motion in the Southern Andes (26°–36°S): Do the Andes behave like a microplate?. *Geochem. Geophys. Geosyst.* **4**, 1085 (2003).
- Horton, B. K. Erosional control on the geometry and kinematics of thrust belt development in the central Andes. *Tectonics* **18**, 1292–1304 (1999).
- Bilham, R. *et al.* GPS measurements of present-day convergence across the Nepal Himalaya. *Nature* **386**, 61–64 (1997).
- Echavarría, L., Hernández, R., Allmendinger, R. & Reynolds, J. Subandean thrust and fold belt of northwestern Argentina; geometry and timing of the Andean evolution. *AAPG Bull.* **87**, 965–985 (2003).
- Uba, C., Kley, J., Strecker, M. & Schmitt, A. K. Unsteady evolution of the Bolivian Subandean thrust belt: The role of enhanced erosion and clastic wedge progradation. *Earth Planet. Sci. Lett.* **281**, 134–146 (2009).
- Hsu, Y. J. *et al.* Spatio-temporal slip, and stress level on the faults within the Western Foothills of Taiwan: Implications for fault frictional properties. *Pure Appl. Geophys.* **166**, 1853–1884 (2009).
- Kumar, S. *et al.* Paleoseismic evidence of great surface rupture earthquakes along the Indian Himalaya. *J. Geophys. Res.* **111** (2006).
- Scholz, C. J. Earthquakes and friction laws. *Nature* **391**, 37–42 (1998).
- Currie, C. A. & Hyndman, R. D. The thermal structure of subduction zone back arcs. *J. Geophys. Res.* **111**, B08404 (2006).
- Lavé, J. & Avouac, J. P. Active folding of fluvial terraces across the Siwalik Hills (Himalaya of central Nepal). *J. Geophys. Res.* **105**, 5735–5770 (2000).
- Lavenue, A. *et al.* *Maps and Database of Quaternary Faults in Bolivia and Chile*. US Geological Survey Open-File Report 00-0283 (2000).
- Scholz, C. H. A reappraisal of large earthquake scaling. *Bull. Seismol. Soc. Am.* **84**, 215–218 (1994).
- Das, S. & Aki, K. Fault plane with barriers—versatile earthquake model. *J. Geophys. Res.* **82**, 5658–5670 (1977).
- Dimate, C. *et al.* Seismic hazard assessment in the Northern Andes (PILOTO Project). *Ann. Geofis.* **42**, 1039–1055 (1999).
- Dahlen, F. A. Critical taper model of fold-and-thrust belts and accretionary wedges. *Annu. Rev. Earth Planet. Sci.* **18**, 55–99 (1990).
- Insel, N. *et al.* Spatial and temporal variability in denudation across the Bolivian Andes from multiple geochronometers. *Geomorphology* **122**, 65–77 (2010).
- Strecker, M. R. *et al.* Tectonics and climate of the southern Central Andes. *Annu. Rev. Earth Planet. Sci.* **35**, 747–787 (2007).

Acknowledgements

This study was supported by the National Science Foundation (grant EAR-0948615) and by Repsol S.A. We thank R. Giraud, D. Demurro, and R. Limachi of Repsol for assistance with field logistics. We gratefully acknowledge the many people who helped with field work, including D. Caccamise, R. Tinta, C. Distanto, T. Ericksen, D. Raleigh, G. Cabrera, A. Mollericon, R. Jauregui, R. Cavero, M. Zamora and O. Ozcacha. We thank J.-P. Avouac for his careful reading and suggestions that significantly improved this manuscript. GMT software was used to prepare the figures.

Author contributions

B.A.B. designed the study, collected GPS data, processed GPS data, performed all analyses and wrote the paper. M. Bevis contributed to the study design, GPS processing approach and data collection. K.W. and J.R.A. contributed to geomorphic analysis. J.F. contributed to the GPS processing approach. T.Z. contributed to the study design and geological interpretation. E.K. collected GPS data and contributed to the GPS processing approach. E.M. contributed to regional seismological analysis. A.E. contributed to the study design and GPS data collection. M. Blanco, P.E., M.S., and R.J.S. Jr collected GPS data. All authors discussed the results and commented on the paper.

Additional information

The authors declare no competing financial interests. Supplementary information accompanies this paper on www.nature.com/naturegeoscience. Reprints and permissions information is available online at <http://www.nature.com/reprints>. Correspondence and requests for materials should be addressed to B.A.B.

Supplementary Information: Orogenic wedge deformation and potential for great earthquakes in the central Andean backarc

Benjamin A. Brooks¹, Michael Bevis², Kelin Whipple³, J Ramon Arrowsmith³, James Foster¹, Tomas Zapata⁴, Eric Kendrick², Estella Minaya⁵, Arturo Echalar⁶, Mauro Blanco⁷, Pablo Euillades⁷, Mario Sandoval⁶, Robert J. Smalley Jr.⁸

¹*School of Ocean and Earth Science and Technology, University of Hawaii, 1680 East-West Rd., Honolulu, HI 96822, USA*

²*School of Earth Sciences, The Ohio State University, 125 S. Oval Mall, Columbus OH 43210, USA*

³*School of Earth and Space Exploration, Arizona State University, P.O. Box 871404, Tempe, AZ 85287, USA*

⁴*YPF Services USA, 1330 Lake Robbins Drive, Box 10, The Woodlands, TX 77380*

⁵*Observatorio San Calixto, Calle Indaburo 944, Casilla 12656, La Paz, Bolivia*

⁶*Instituto Geografico Militar, Av Saavedra 2303, La Paz, Bolivia*

⁷*Instituto CEDIAC, Universidad Nacional de Cuyo, Centro Universitario, Parque General San Martín. CC 405 - (5500) Mendoza, Argentina*

⁸*Center for Earthquake Research and Information, The University of Memphis, 3876 Central Ave., Suite 1, Memphis, TN 38152-3050*

S1 GPS Processing

The new GPS solution includes sites initially installed from 2000 to 2003 and we present velocity estimates for only those stations with total time-span of more than ~3 years. Our field, processing, and velocity analysis methods in South America have been described previously ¹⁻⁸. We estimate velocities by stacking daily network solutions (polyhedra) obtained using GAMIT ⁹ and GLOBK ¹⁰ software. We express our velocities in a reference frame nominally attached to the stable South American craton that has a horizontal RMS velocity of less than 1 mm/yr (Table S1, Figure S1). We estimate positions and velocities in inner coordinates, treating the reference frame as a computational convenience and allowing it to rotate and translate freely (at constant rates) while focusing on the rate of change of the polyhedron's shape and size. One six parameter Helmert transformation is applied to each daily polyhedron solution so as to align the daily polyhedra as closely as possible to a suite of constant velocity trajectories. No position or velocity constraints are imposed during this iterative stacking process: the only constraint is that the individual (daily) polyhedra are not allowed to change their size or shape.

S2 Dislocation Modeling and Inversion

To compare with GPS-estimated velocities, we explore a model that explains the GPS velocity field due to continuous, uniform slip on a buried dislocation in an elastic half space ¹¹. We assume a standard Poisson's ratio of 0.25. Although this is a simplification of

the depth-variable rheology that surely characterizes the Central Andean Plateau's east flank, via favorable comparisons with finite-element models this approach has been shown to be valid for modeling the surface displacements and stress distributions associated with large intracontinental thrust faults ¹².

We project the GPS velocity data into a Transverse Mercator projection so that the Chile trench is parallel to the y axis ⁴ and use the Gibbs Sampling Heat Bath method, a Monte-Carlo based technique, that allows robust searching of multidimensional parameter space ¹³, to compare the model to the horizontal velocities. Although this non-linear inverse problem typically has 9 free parameters (dislocation upper left corner x, y , and z position; dislocation length, width, depth, strike, and dip; magnitude of strike-slip and dip-slip) we reduce that number to 6 by assuming that the dislocation is very long (along-strike) and wide (across-strike): y position is held fixed, and length and width are taken to be very large. In this case, the distance from the thrust front to the dislocation's upper left corner x coordinate is the locking width W_L .

S3 Erosional Flux Calculations

Insel et al. (2010) present denudation rates from the SSA from a compilation of published and new rates determined from low-temperature thermochronology ('long-term' rates, $> 10^6$) and cosmogenic radionuclide analysis ('medium-term' rates, $10^2 - 10^4$ years) (Fig. SI 2a). From these data we estimate erosional flux, F_E , by numerically integrating the denudation rates across a specified distance (Fig. SI 2b). If we use all of the data presented

by Insel et. al (2010) then medium-term F_E is $55\text{m}^2/\text{yr}$ and long-term F_E is $58\text{m}^2/\text{yr}$. Because our goal, however, is to evaluate the mass balance of the SSA alone, we also make estimates for only those data sampled from within the SSA (Fig. SI 2b). This yields medium-term F_E of $50\text{m}^2/\text{yr}$ and long-term F_E of $17\text{m}^2/\text{yr}$. We note that the long-term rates do not fully sample the entire SSA, only its western half and so we use the medium-term rates in our comparison with F_A . This is a reasonable approach for the region given that in the northern Subandes, as noted by Insel et al. (2010), medium-term erosion rates are within the range of long-term rates¹⁵. Moreover, the $50\text{m}^2/\text{yr}$ value is conservative given that we wish to compare it with accretionary flux values, F_A , of $\sim 70\text{-}130\text{ m}^2/\text{yr}$ (see main text).

S4 Mandeyapecua Thrust Fault Topographic Analysis

The Mandeyapecua thrust fault (MTF) is the west-dipping frontal thrust of the Central Andes in Bolivia and it has been associated with Quaternary displacement^{16,17}. The recent trace of the MTF is clearly delineated in SRTM (90 m posting) data from the SSA (Figure SI 3-8) and we have verified this with field visits to selected locales. Recent scarps of 10-50m height are visible in the SRTM data from near the town of Charagua (Fig. SI 8) and the magnitude of MTF topographic relief reaches as much as $\sim 125\text{m}$ at various places along its length (Fig. SI 3-7).

Because of its clear tectonic origin (the scarps are oriented perpendicular to major rivers), and because seismic imaging identifies the MTF as a ramp associated with the

decollement^{17,18}, MTF along-strike segmentation can be used as a proxy for the long-term slip distribution on the decollement¹⁹. We quantify this by calculating the relief associated with the MTF topographic scarp defined as the difference in median values of sampled topography in the hangingwall (west) and footwall (eastern). Sampling is done in boxes 5km along-strike by 8km (4km on each hangingwall and footwall) across-strike. The sampling boxes and their relationship to the MTF scarps are displayed in Figure SI 3-7.

S5 Earthquake Rupture Parameter Estimation

We estimate potential rupture parameters for two classes of earthquakes associated with the MTF: 1) events that rupture the entire along-strike extent of the MTF, and 2) events that rupture individual segments.

For the case where the entire fault ruptures, we assume that slip initiates at the slipping-locked transition and extends up-dip on the decollement to the thrust front. In this case, because the entire thickness of the seismogenic crust ruptures, we use the scaling relations for ‘large’ intraplate thrust earthquakes^{20,21}. For each dislocation solution we calculate maximum slip (Figure 4d) by using the empirically-determined ratio of: $d_{max}/W = 10^{-4}$, where W is our estimate locked width, W_L . Slip-rate is taken directly from the inversion slip estimates and the recharge time (t_r , Figure 4f) is the amount of time needed to accumulate d_{max} . Seismic moment, M_0 , is calculated from d_{max} , L , and W_L with the standard definition: $M_0 = \mu(L*W_L) d_{max}$ assuming $\mu = 30$ GPa and then, $M_W = (\log M_0 - 16.05) / 1.5^{22}$.

For the case where individual segments rupture, we consider two end-member scenarios based on rupture scaling dimensions of 4:1 and 1:1 ($L:W$) (Table SI 2). From the segment length we calculate rupture width, W_{min} (4:1, $L:W$) and W_{max} (1:1, $L:W$) and then, as above, find d_{max} , M_W , and t_r . For the Charagua segment, W_{max} for the 1:1 rupture is greater than the maximum estimated locking width, W_L (138km) , so we use the 138 km value.

References

- 1 Bevis, M. *et al.* Blending Old and New Approaches to Regional Geodesy. *Eos, Transactions, American Geophysical Union* 78, 61,64-66 (1997).
- 2 Bevis, M. *et al.* On the strength of interplate coupling and the rate of back arc convergence in the central Andes: An analysis of the interseismic velocity field. *Geochemistry, Geophysics, Geosystems* 2, 2001GC000198 (2001).
- 3 Bevis, M. *et al.* Crustal motion north and south of the Arica deflection: Comparing recent geodetic results from the Central Andes. *Geochemistry, Geophysics, Geosystems* 1, 1999GC000011 (1999).
- 4 Brooks, B. *et al.* Crustal Motion in the Southern Andes (26-36S): Do the Andes Behave Like a Microplate? *Geochemistry, Geophysics, Geosystems* 4, 2003GC000505 (2003).
- 5 Kendrick, E., Bevis, M., Smalley, R. J. & Brooks, B. An integrated crustal velocity field for the central Andes. *Geochemistry, Geophysics, Geosystems* 2 (2001).
- 6 Kendrick, E. *et al.* The Nazca-South America Euler Vector and its Rate of Change. *Journal of South American Earth Sciences* 16, 125-131 (2003).
- 7 Kendrick, E. *et al.* Active Orogeny of the South-Central Andes Studied with GPS Geodesy. *Rev. Asoc. Geol. Argent.* 61, 555-566 (2006).
- 8 Kendrick, E. C., Bevis, M., Smalley, R. F., Jr., Cifuentes, O. & Galban, F. Current rates of convergence across the Central Andes; estimates from continuous GPS observations. *Geophysical Research Letters* 26, 541-544 (1999).
- 9 King, R. & Bock, Y. *Documentation for the GAMIT GPS Analysis Software*, (2000).

- 10 Herring, T. *Documentation for GLOBK: Global KalmanFilter VLBI and GPS analysis program*, 2000)
- 11 Okada, Y. Surface deformation due to shear and tensile faults in a half-space. *Bulletin of the Seismological Society of America* 75, 1135-1154 (1985).
- 12 Vergne, J., Cattin, R. & Avouac, J. P. On the use of dislocations to model interseismic strain and stress build-up at intracontinental thrust faults. *Geophys. J Int.* 147, 155-162 (2001).
- 13 Brooks, B. A. & Frazer, L. N. Importance reweighting reduces dependence on temperature in Gibbs samplers: an application to the coseismic geodetic inverse problem. *Geophys. J Int.* 161, 12-21 (2005).
- 14 Insel, N. *et al.* Spatial and temporal variability in denudation across the Bolivian Andes from multiple geochronometers. *Geomorphology* 122, 65-77, [j.geomorph.2010.05.014](https://doi.org/10.1016/j.geomorph.2010.05.014) (2010).
- 15 Safran, E. B. *et al.* in *Earth Surface Processes and Landforms* (eds A.M. Heimsath & T.A. Ehlers) 1007–1024 (2005).
- 16 Lavenu, A. *et al.* Maps and Database of Quaternary Faults in Bolivia and Chile. *U.S. Geological Survey Open-File Report 00-0283* (2000).
- 17 Moretti, I., Baby, P., Mendez, E. & Zubieta, D. Hydrocarbon generation in relation to thrusting in the Sub Andean Zone from 18 to 22 S, Bolivia. *Petroleum Geoscience* 2, 17-28 (1996).

- 18 Uba, C., Kley, J., Strecker, M. & Schmitt, A. K. Unsteady evolution of the Bolivian Subandean thrust belt: The role of enhanced erosion and clastic wedge progradation. *Earth and Planetary Science Letters* 281, 134-146 (2009).
- 19 Burbank, D. & Anderson, R. S. *Tectonic Geomorphology*. (Blackwell Science, 2001).
- 20 Scholz, C. H. Size Distributions for Large and Small Earthquakes. *Bulletin of the Seismological Society of America* 87, 1074-1077 (1997).
- 21 Scholz, C. H. A Reappraisal of Large Earthquake Scaling. *Bulletin of the Seismological Society of America* 84, 215-218 (1994).
- 22 Hanks, T. C. & Kanamori, H. A moment-magnitude scale. *Journal of Geophysical Research* 84, 2348-2350 (1979).

Table SI-1. GPS-derived velocities. Stnm, station name (asterisk denotes reference frame station); Long, longitude; Lat, latitude; Ve, east component of velocity; Vn, north component; sigVe, standard error east component; sigVn, standard error north component; neCor, north-east correlation; tspan, time-span.

Table SI-2. Earthquake rupture estimates derived for each MTF segment. Length, distance between relief minima (see Fig. 4b); rupture width, W_{max} (1:1, L:W ratio); W_{min} (4:1, L:W ratio); co-seismic slip, D_{max} (1:1, L:W ratio); D_{min} (4:1, L:W ratio); M_W (1:1, L:W ratio); M_W (4:1, L:W ratio); recharge time, T_{max} (1:1, L:W ratio); M_{min} (4:1, L:W ratio).

Figure SI-1. South American reference frame stations and horizontal velocities.

Figure SI-2. Denudation rate sample locations and values. (A) Location map of SSA denudation rate estimates taken from Insel *et al.* (2010), table 1. Red, medium-term (10^2 - 10^4) years; blue, long-term ($> 10^6$) years. (B) Rates from (A), color-coded accordingly, plotted versus distance (km) from the AP/EC limit. The inset shows calculated F_e from numerical integration of the data.

Figure SI-3-7. SRTM topography of Mandeyapecua Thrust Fault segments used to create the relief profile from Figure 3b. Black boxes are the sampling boxes used in the relief calculations. SI-3, Yacuiba segment; SI-4, Ibibobo; SI-5, Villamontes; SI-6, Charagua; SI-7, Santa Cruz.

Figure SI-8. Grey-scale shaded relief SRTM topography of MTF near Charagua showing evidence for recent faulting. Arrows denote young fault scarp with offsets identified.

Supplemental Table 1

| <u>Stnm</u> | <u>Long</u> | <u>Lat</u> | <u>Ve</u> | <u>Vn</u> | <u>sigVe</u> | <u>sigVn</u> | <u>neCor</u> | <u>tspan</u> |
|-------------|-------------|------------|-----------|-----------|--------------|--------------|--------------|--------------|
| ASLO | -64.16734 | -19.52319 | 5.5 | -5.6 | 0.47 | 0.38 | -0.4214 | 9.158 |
| BLSK | -64.70601 | -21.56406 | 8.1 | 2.6 | 0.22 | 0.28 | -0.0835 | 3.047 |
| BRAZ* | -47.87787 | -15.94747 | -0.7 | 0 | 0.04 | 0.02 | -0.0007 | 9.997 |
| CAGA | -63.22417 | -19.7902 | 1.2 | 0.4 | 2.11 | 3.44 | 0.0753 | 9.112 |
| CCDO | -62.38075 | -19.43908 | 0.9 | 0.7 | 0.81 | 0.97 | -0.1689 | 9.101 |
| CMRI | -63.54245 | -20.07124 | 2 | 1 | 0.26 | 0.19 | -0.135 | 9.15 |
| DRDO | -64.34982 | -19.29682 | 8.7 | 2.1 | 0.76 | 1.19 | -0.1563 | 9.161 |
| EISL | -109.38329 | -27.14821 | 65 | -10.6 | 0.03 | 0.03 | 0.1706 | 9.997 |
| ENRI | -64.22803 | -21.46776 | 5 | 2.7 | 0.86 | 0.63 | -0.2844 | 2.84 |
| FORT* | -38.42561 | -3.87745 | 0.3 | -0.2 | 0.11 | 0.04 | 0.0642 | 6.266 |
| KOUR* | -52.80596 | 5.25218 | 0 | 1.1 | 0.05 | 0.02 | 0.0067 | 9.997 |
| LKTH* | -57.85074 | -51.69841 | 0 | 0 | 0.03 | 0.04 | -0.2626 | 7.529 |
| LPGS* | -57.9323 | -34.90675 | 0.4 | -0.6 | 0.03 | 0.03 | -0.1305 | 9.997 |
| M007 | -63.90083 | -21.39533 | 3 | -0.5 | 1.03 | 0.66 | 0.287 | 6.115 |
| M009 | -62.88768 | -21.57024 | 2.7 | 0.2 | 1.03 | 0.66 | 0.287 | 6.112 |
| M010 | -62.75844 | -21.64094 | 1 | 0 | 1.03 | 0.66 | 0.287 | 6.115 |
| M011 | -63.12103 | -21.44561 | 2 | -0.9 | 1.03 | 0.66 | 0.287 | 6.09 |
| M012 | -63.22953 | -21.36198 | 1.5 | -1.3 | 0.16 | 0.25 | -0.0103 | 6.085 |
| MARG | -63.75201 | -21.12913 | 6 | -0.9 | 0.16 | 0.14 | -0.35 | 6.233 |
| PARA | -49.23095 | -25.44837 | -0.3 | -0.5 | 0.05 | 0.03 | 0.0166 | 7.337 |
| PBOL | -62.62942 | -21.56185 | 1.6 | -0.3 | 0.2 | 0.16 | -0.5604 | 6.121 |
| SALA | -62.98488 | -19.61862 | 1.8 | 1.4 | 1.09 | 0.73 | -0.0059 | 4.23 |
| SUCE | -65.30262 | -19.00621 | 7.2 | 3.3 | 0.1 | 0.07 | -0.1746 | 3.953 |
| SUCR | -65.20603 | -18.99209 | 10.4 | 2 | 0.77 | 0.7 | -0.0129 | 6.892 |
| TARI | -65.0479 | -21.63067 | 9.6 | 1 | 0.52 | 0.51 | -0.0518 | 9.032 |
| TPYO | -63.95453 | -21.3247 | 6 | 0.3 | 0.15 | 0.14 | -0.2633 | 6.219 |
| TRJA | -64.71652 | -21.54948 | 6.5 | 0.3 | 0.25 | 0.2 | -0.2939 | 1.833 |

| | | | | | | | | |
|-------|-----------|-----------|------|-----|------|------|---------|-------|
| UEPP* | -51.40853 | -22.1199 | 0.3 | 0.2 | 0.07 | 0.05 | -0.0805 | 5.885 |
| UYNI | -66.82596 | -20.46595 | 11.1 | 2.3 | 0.08 | 0.08 | -0.2624 | 3.89 |
| VMON | -63.48355 | -21.25894 | 1.5 | 0.9 | 0.14 | 0.14 | -0.3134 | 6.395 |
| ZDNZ | -64.69797 | -19.12341 | 9.7 | 2.6 | 0.81 | 0.72 | -0.0894 | 9.158 |

Supplemental Table 2

| <u>Name</u> | <u>Length(km)</u> | <u>Wmax(km)</u> | <u>Wmin(km)</u> | <u>Dmax(m)</u> | <u>Dmin(m)</u> | <u>Mw(max)</u> | <u>Mw(min)</u> | <u>Tmax(yrs)</u> | <u>Tmin(yrs)</u> |
|-------------|-------------------|-----------------|-----------------|----------------|----------------|----------------|----------------|------------------|------------------|
| Yacuiba | 66.8 | 66.8 | 16.7 | 6.7 | 1.7 | 7.9 | 7.1 | 667.7 | 166.9 |
| Ibibobo | 97 | 97 | 24.2 | 9.7 | 2.4 | 8.3 | 7.5 | 969.5 | 242.4 |
| Villamontes | 125.3 | 125.3 | 31.3 | 12.5 | 3.1 | 8.5 | 7.7 | 1253 | 313.3 |
| Charagua | 155.5 | 138 | 38.9 | 13.8 | 3.9 | 8.6 | 7.9 | 1380 | 388.7 |
| Santa Cruz | 132.6 | 132.6 | 33.2 | 13.3 | 3.3 | 8.5 | 7.7 | 1326.2 | 331.6 |

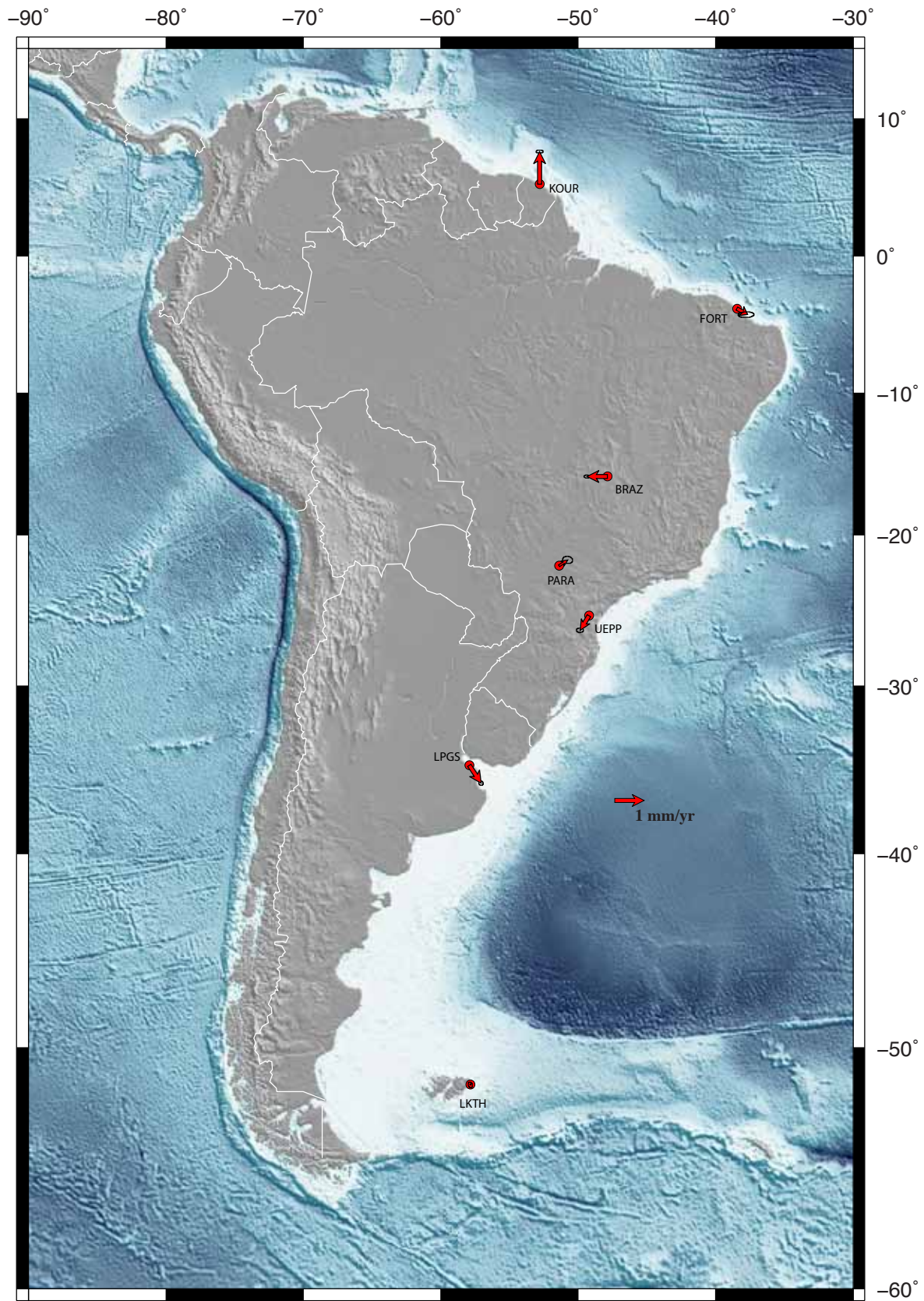


Figure SI 1

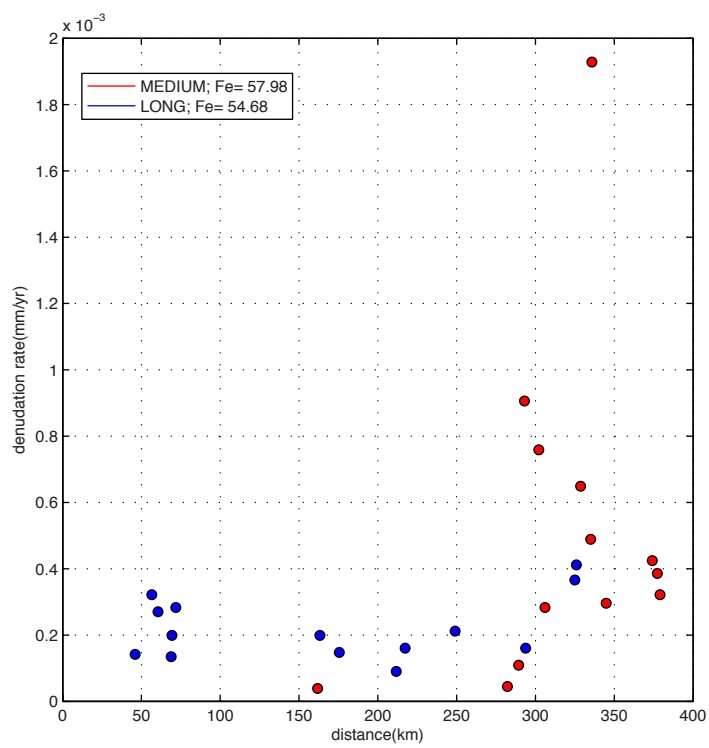
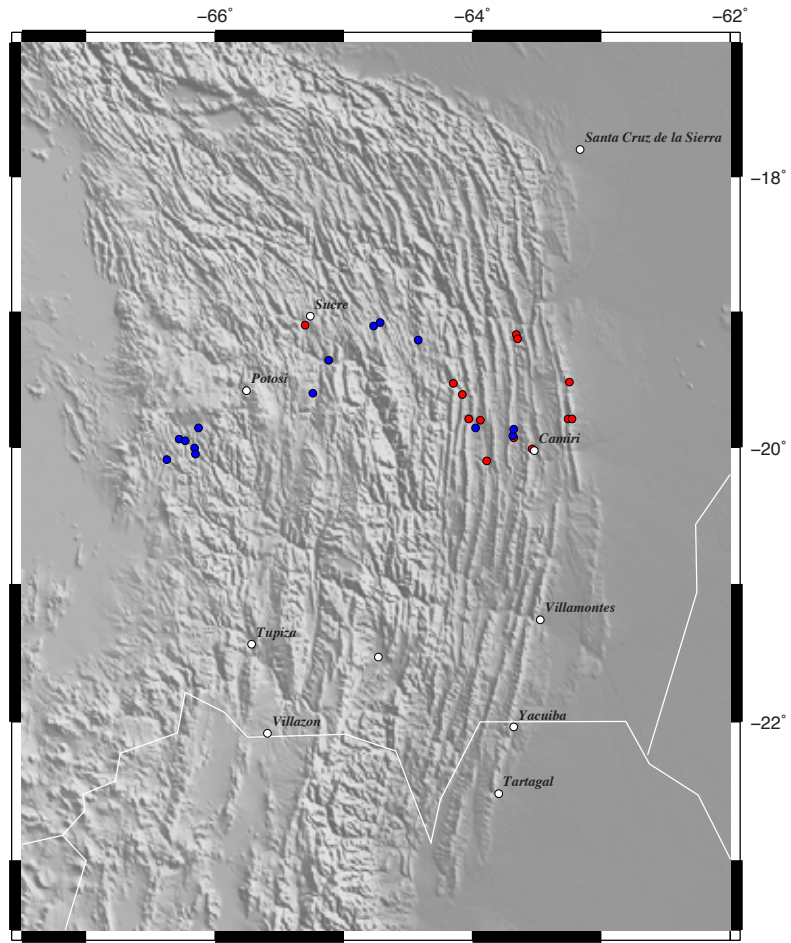


Figure SI 2

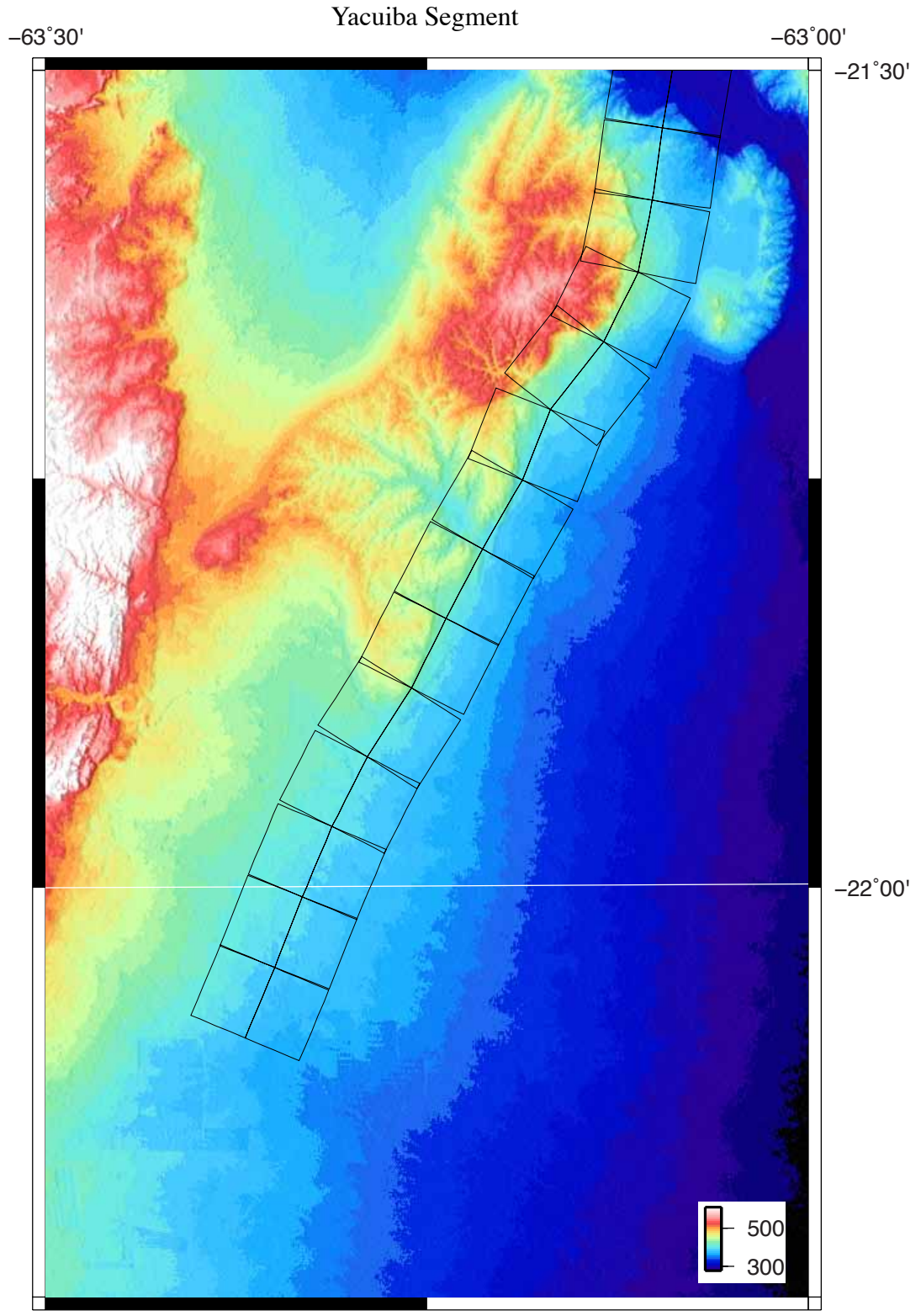


Figure SI 3

Ibibobo Segment

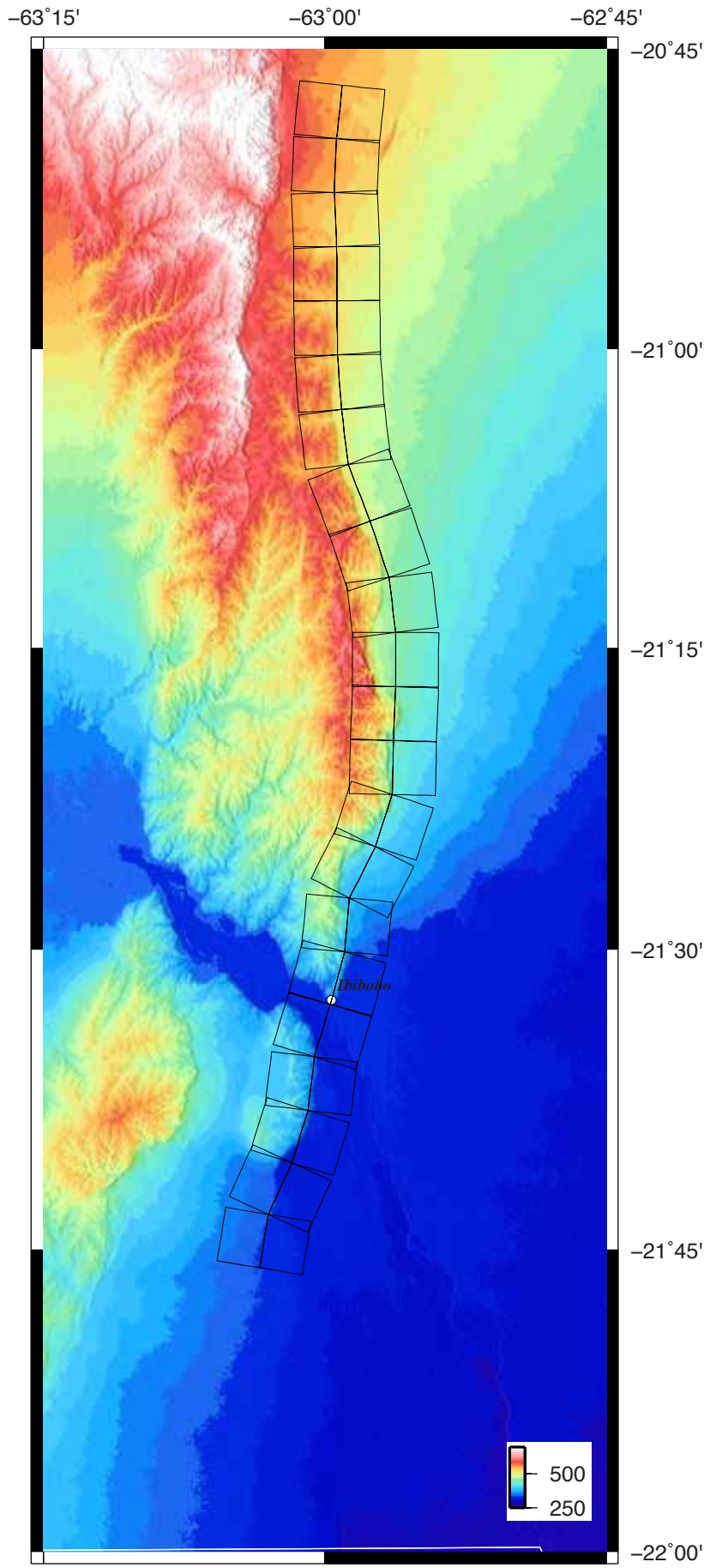


Figure SI 4

Villamontes Segment

-63°00'

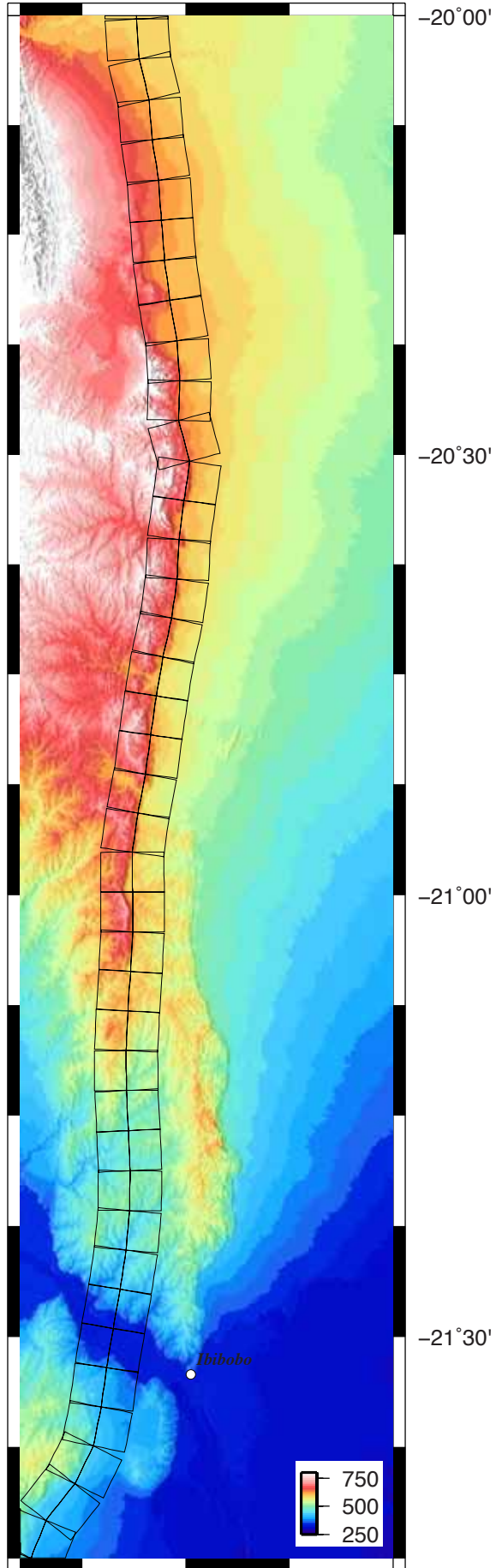


Figure SI 5

Charagua Segment

-63°00'

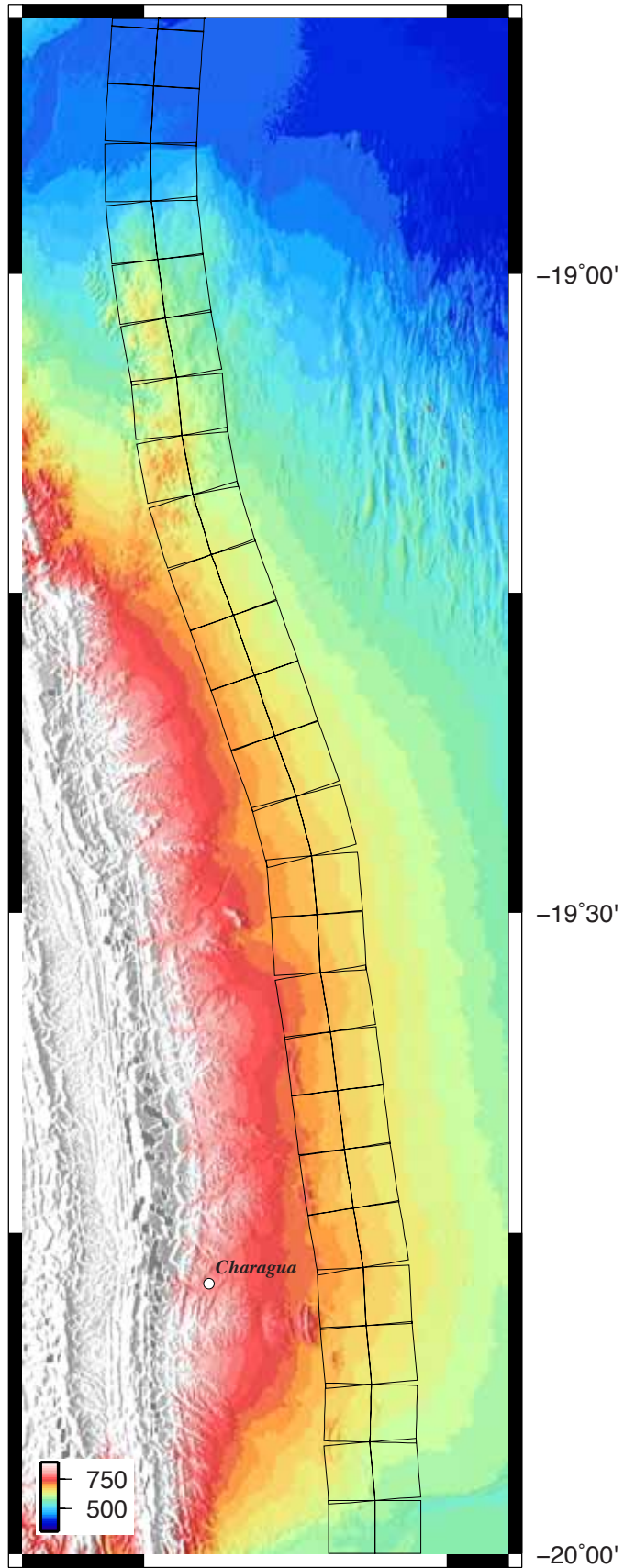


Figure SI 6

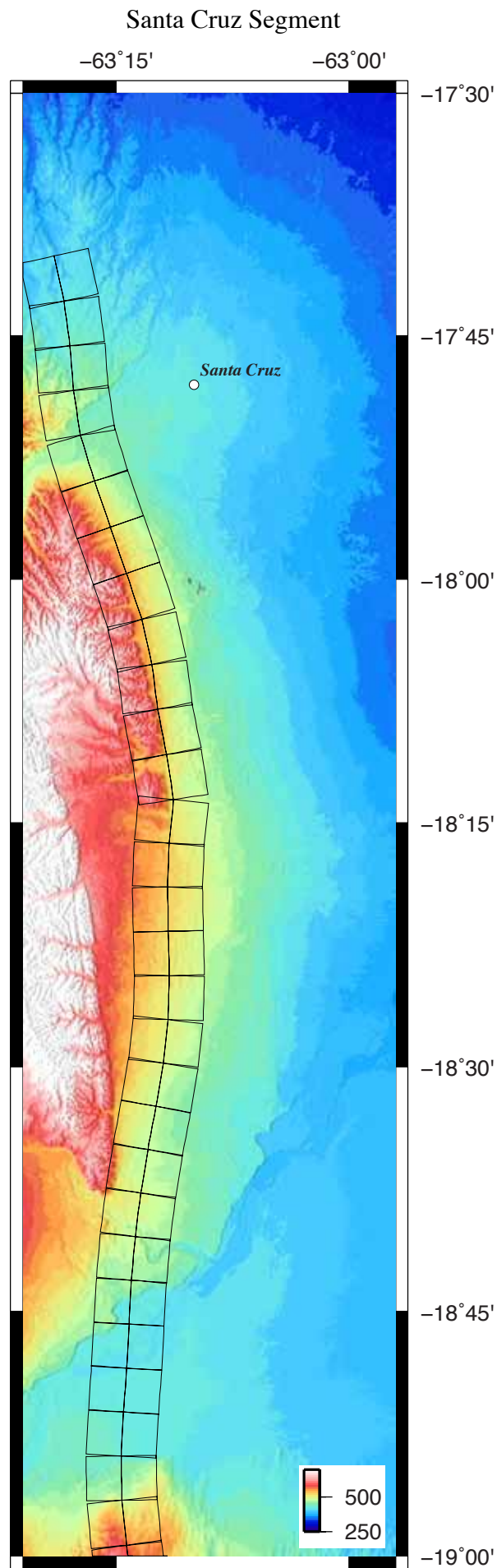


Figure SI 7

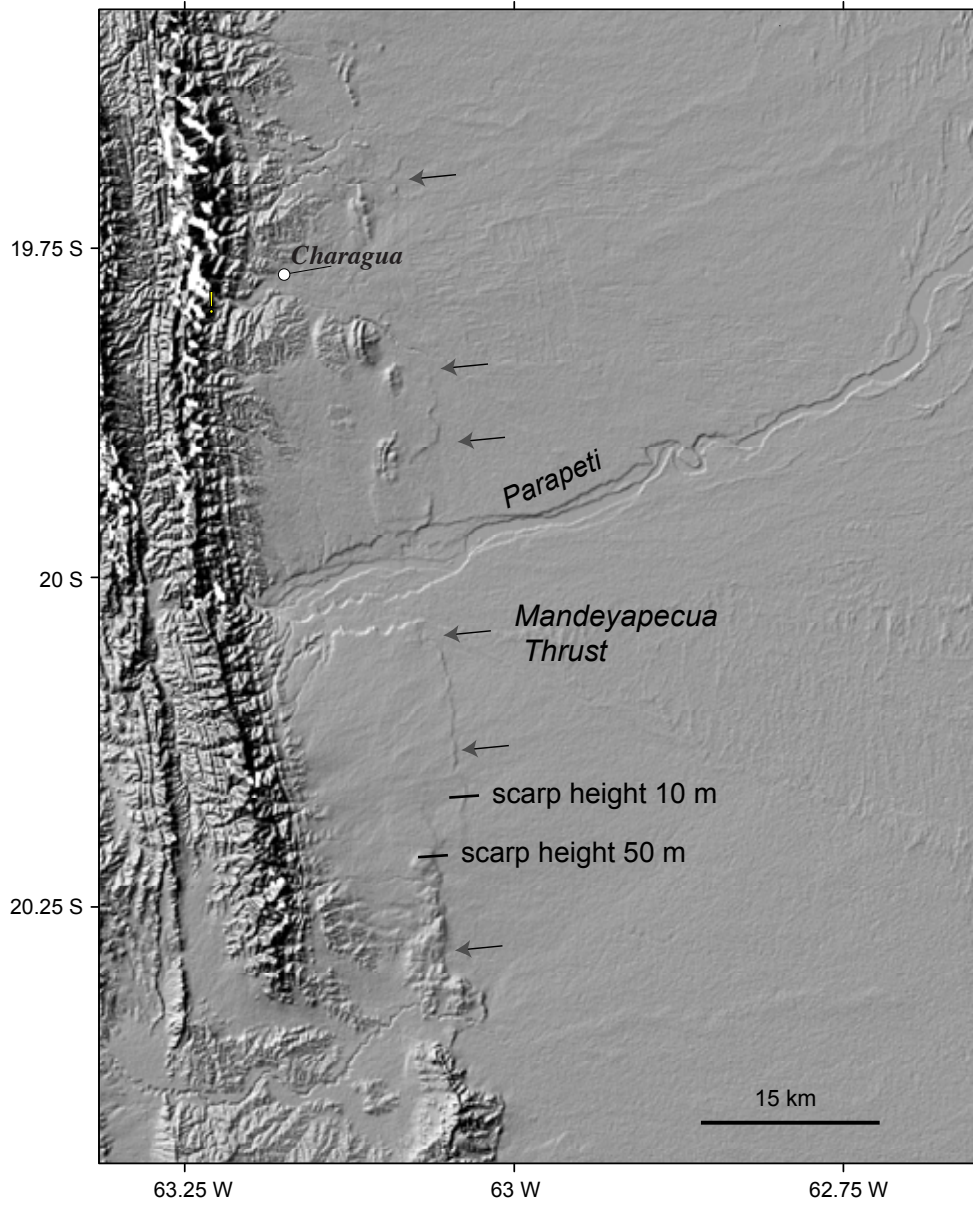


Figure SI 8